

Modified Oxygen Defect Chemistry at Transition Metal Oxide Heterostructures Probed by Hard X-ray Photoelectron Spectroscopy and X-ray Diffraction

Yan Chen,^{†,‡,§} Dillon D. Fong,^{||} F. William Herbert,^{†,§} Julien Rault,[⊥] Jean-Pascal Rueff,^{⊥,#} Nikolai Tsvetkov,^{†,‡} and Bilge Yildiz^{*,†,‡,§}

[†]Laboratory of Electrochemical Interfaces, [‡]Department of Nuclear Science and Engineering, [§]Department of Materials Science and Engineering, Massachusetts Institute of Technology, Cambridge, Massachusetts 02139, United States

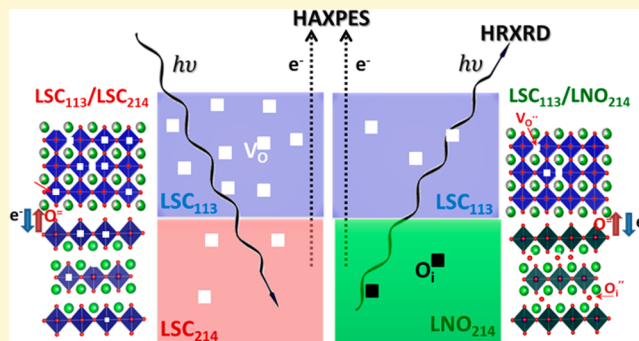
^{||}Materials Science Division, Argonne National Laboratory, Argonne, Illinois 60439, United States

[⊥]Synchrotron SOLEIL, l'Orme des Merisiers, Saint-Aubin, France

[#]Sorbonne Universités, UPMC Univ Paris 06, CNRS, Laboratoire de Chimie Physique – Matière et Rayonnement, 11 rue Pierre et Marie Curie, 75005 Paris, France

Supporting Information

ABSTRACT: Transition metal oxide heterostructures are interesting due to the distinctly different properties that can arise from their interfaces, such as superconductivity, high catalytic activity, and magnetism. Oxygen point defects can play an important role at these interfaces in inducing potentially novel properties. The design of oxide heterostructures in which the oxygen defects are manipulated to attain specific functionalities requires the ability to resolve the state and concentration of local oxygen defects across buried interfaces. In this work, we utilized a novel combination of hard X-ray photoelectron spectroscopy (HAXPES) and high resolution X-ray diffraction (HRXRD) to probe the local oxygen defect distribution across the buried interfaces of oxide heterolayers. This approach provides a nondestructive way to qualitatively probe locally the oxygen defects in transition metal oxide heterostructures. We studied two trilayer structures as model systems: the $\text{La}_{0.8}\text{Sr}_{0.2}\text{CoO}_{3-\delta}/(\text{La}_{0.5}\text{Sr}_{0.5})_2\text{CoO}_{4-\delta}/\text{La}_{0.8}\text{Sr}_{0.2}\text{CoO}_{3-\delta}$ ($\text{LSC}_{113}/\text{LSC}_{214}$) and the $\text{La}_{0.8}\text{Sr}_{0.2}\text{CoO}_{3-\delta}/\text{La}_2\text{NiO}_{4+\delta}/\text{La}_{0.8}\text{Sr}_{0.2}\text{CoO}_{3-\delta}$ ($\text{LSC}_{113}/\text{LNO}_{214}$) on SrTiO_3 (001) single crystal substrates. We found that the oxygen defect chemistry of these transition metal oxides was strongly impacted by the presence of interfaces and the properties of the adjacent phases. Under reducing conditions, the LSC_{113} in the $\text{LSC}_{113}/\text{LNO}_{214}$ trilayer had less oxygen vacancies than the LSC_{113} in the $\text{LSC}_{113}/\text{LSC}_{214}$ trilayer and the LSC_{113} single phase film. On the other hand, LSC_{214} and LNO_{214} were more reduced in the two trilayer structures when in contact with the LSC_{113} layer compared to their single phase counterparts. The results point out a potential way to modify the local oxygen defect states at oxide heterointerfaces.



1. INTRODUCTION

Ionic defects, particularly oxygen defects, are known to affect the properties of transition metal oxides.^{1–3} Controlling oxygen defects electrochemically^{4–6} may pave the way to modifying the magnetic, electronic, and transport properties of transition metal oxides. The importance of oxygen defects has motivated the development of techniques to quantify their total concentration in bulk materials, such as thermogravimetric analysis (TGA), dilatometry,² and Raman spectroscopy.^{7–9} In addition to their total concentration, it is important to know their spatial distribution near extended defects, such as surfaces, grain boundaries, and heterophase boundaries. Knowing their concentration and structure near the interfaces can allow tuning of the local functionality of the material. Resolving oxygen

defect states near heterointerfaces buried beneath the surface is important for advancing our understanding of the unique properties that arise at such interfaces, including magnetism,¹⁰ electronic conductivity,^{11,12} ionic conductivity,^{13,14} and catalytic activity.^{15–23} Fascinating recent examples include the reversible control of the oxygen defect content by external bias near the Co/GdOx heterointerface to tailor the magnetic anisotropy of Co,¹⁰ and near the interface of $\text{Ti}/\text{Pr}_{1-x}\text{Ca}_x\text{MnO}_3$ metal-oxide layers to reversibly change the charge-carrier transport characteristics for resistive switching.²⁴

Received: February 23, 2018

Revised: April 17, 2018

Published: April 17, 2018

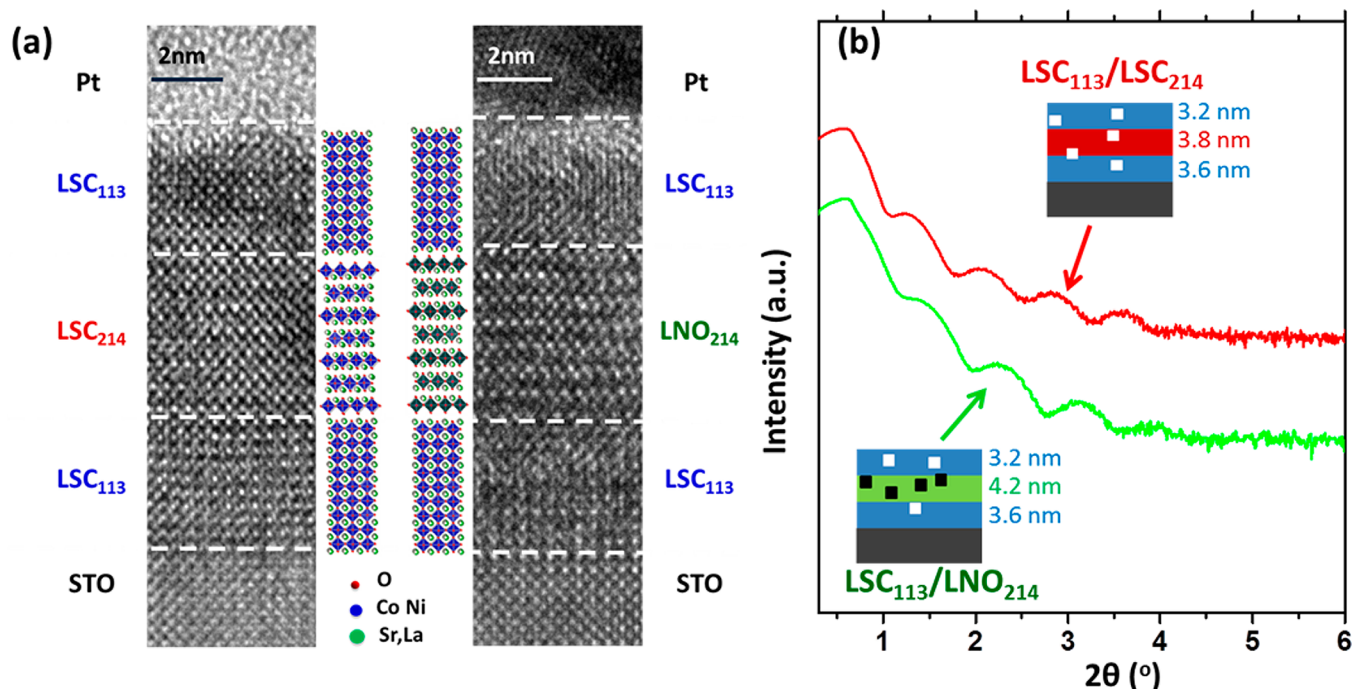


Figure 1. Structure of LSC₁₁₃/LSC₂₁₄ and LSC₁₁₃/LNO₂₁₄ trilayer model systems. (a) Transmission electron microscopy (TEM) images of the trilayer structure. Pt serves as the capping layer for TEM imaging. (b) X-ray reflectivity (XRR) of LSC₁₁₃/LSC₂₁₄ and LSC₁₁₃/LNO₂₁₄ trilayers in their as-prepared state. The inset schematics represent the LSC₁₁₃/LSC₂₁₄ and LSC₁₁₃/LNO₂₁₄ trilayer model structures, in which the black squares and white squares symbolize the oxygen interstitials and oxygen vacancies, respectively.

Obtaining information about local oxygen defect states near the buried heterointerfaces of oxides, however, remains a challenging task. Previous successful attempts include the works of Kim et al.,^{25,26} who used scanning transmission electron microscopy (STEM) to map the oxygen vacancies in oxide thin films based on the changes in local lattice parameters. They reported different oxygen vacancy distributions in (La_{0.5}Sr_{0.5})-CoO₃ films epitaxially grown on NdGaO₃ and (LaAlO₃)_{0.3}(Sr₂AlTaO₆)_{0.7} substrates,²⁵ and this difference in oxygen vacancy concentration was associated with distinct magnetic properties in the two systems studied. The same authors also observed the local accumulation of oxygen vacancies near the BiFeO₃/La_xSr_{1-x}MnO₃ interface,²⁶ and they proposed that these vacancies impact the polarization switching behavior near the interface. The oxidation state of the cation as related to the oxygen defect concentration near buried interfaces can also be obtained by X-ray photoelectron spectroscopy and sputter depth-profiling. For example, Tsvetkov et al.²⁷ performed such analysis across the interface of La_{0.8}Sr_{0.2}CoO_{3-δ}/(La_{0.5}Sr_{0.5})₂CoO_{4-δ}, for which the results were linked to faster oxygen reduction kinetics important for fuel cells. Despite these motivating and successful examples, the destructive nature of the experimental methods may introduce uncertainties in the quantification of the point defects near interfaces. In this work, we implemented a nondestructive approach combining hard X-ray photoelectron spectroscopy (HAXPES)^{28–30} and high resolution X-ray diffraction (HRXRD) to qualitatively probe the spatial distribution of oxygen defects in and across the buried interfaces of thin trilayer model structures. The high energy of photons used in HAXPES enabled probing depths greater than 10 nm, which was comparable to the total thickness of the trilayer samples. By varying the photon energy and the photoelectron emission angle, the oxygen defect content from different depths across the buried interface was

estimated by analyzing the transition metal valence state and the cation composition. Complementary to HAXPES, the lattice parameters measured by HRXRD allowed quantification of the changes in the oxygen defect concentration of each layer. Our approach is nondestructive and can be adapted broadly to other oxide heterolayers to understand the effect of interfaces on oxygen defects, and there by on the unique interface-induced properties.^{11–23}

In this study, we assessed trilayer heterostructures as model systems made of perovskite (ABO₃) and Ruddlesden–Popper (RP) (A'₂B'O₄) oxides. Perovskite and RP oxides have been studied widely for oxygen reduction and oxygen transport in fuel cells and separation membranes.^{31,32} In particular, cobaltite perovskite-RP heterostructures (with B = Co) have attracted great interest recently because they can present significantly enhanced oxygen reduction kinetics compared to their single phase counterparts.^{16–21} The mechanisms behind such an enhancement were studied with both experiments and theoretical calculations^{33–36} for heterostructures of La_{0.8}Sr_{0.2}CoO_{3-δ} (LSC₁₁₃) and (La_{0.5}Sr_{0.5})₂CoO_{4-δ} (LSC₂₁₄), where δ is the oxygen nonstoichiometry. Until now, however, the potential role of oxygen defects at or near these interfaces has been missing from the picture. In this work, we characterized the oxygen defect chemistry near the buried interfaces between LSC₁₁₃ and two RP-type oxides that have very different oxygen defect chemistries: LSC₂₁₄ and La₂NiO_{4+δ} (LNO₂₁₄). At the experimental conditions in this work, the dominant oxygen defects in single phase LSC₂₁₄ are oxygen vacancies, and in LNO₂₁₄ oxygen interstitials. These two heterostructures in the form of trilayers on single crystal SrTiO₃ (STO) (001) are denoted as LSC₁₁₃/LSC₂₁₄ and LSC₁₁₃/LNO₂₁₄, respectively. We found that the LSC₁₁₃ with LNO₂₁₄ is less reducible than the LSC₁₁₃ alone or the LSC₁₁₃ with LSC₂₁₄. On the other hand, the LSC₂₁₄ and LNO₂₁₄ lose oxygen more

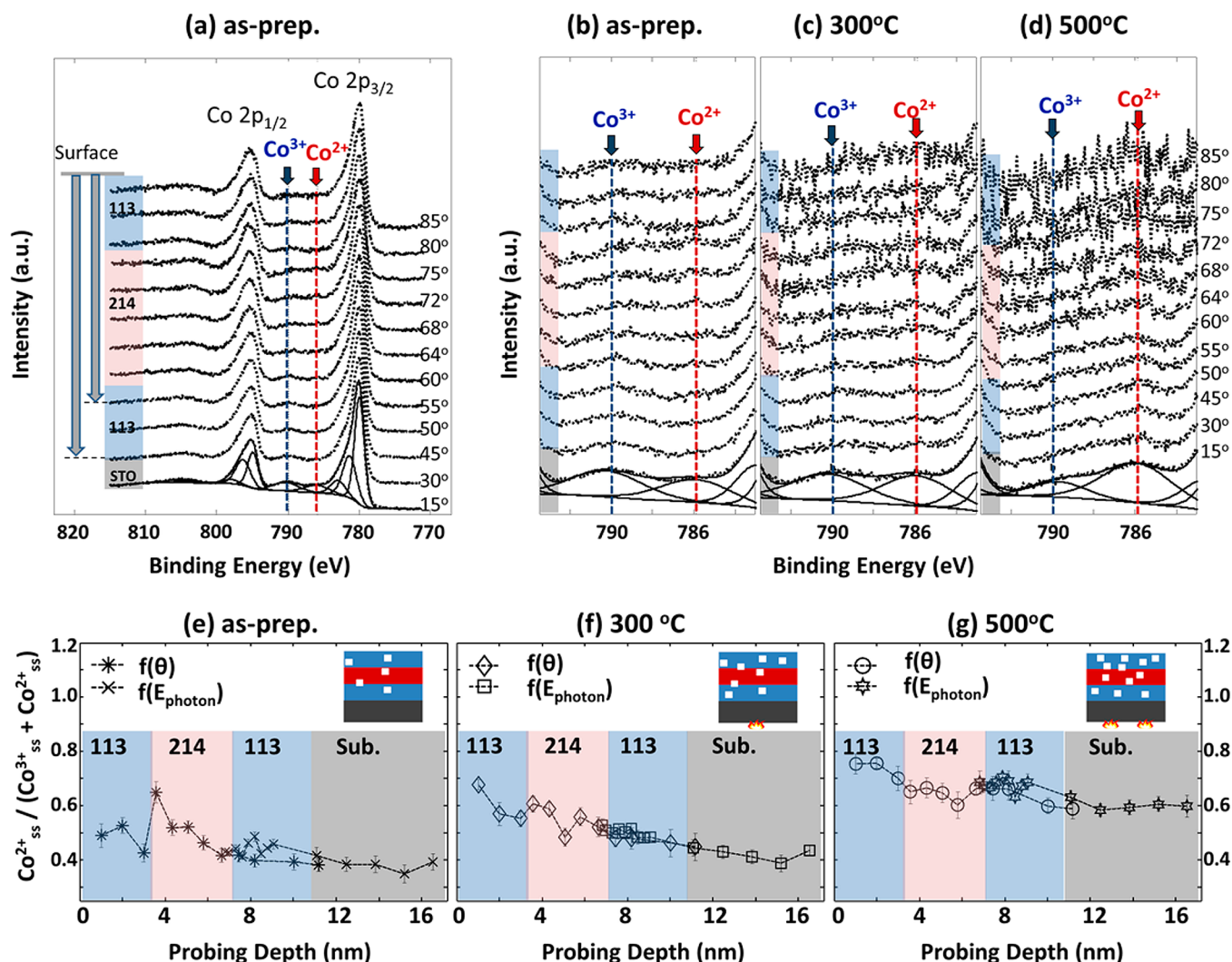


Figure 2. Depth profile of Co valence state in the trilayer thin films. (a) Representative Co 2p spectra collected with photon energy of 3000 eV as a function of emission angle from 85° to 15°, shown for the as-prepared LSC₁₁₃/LSC₂₁₄ trilayer. Each spectra contain cumulative information extending from the surface to the probing depth, as marked by the gray arrow (the length of arrow is not to scale). (b–d) Comparison of the shape of the Co 2p_{3/2} satellite peak in LSC₁₁₃/LSC₂₁₄ among the (b) as-prepared state, and after annealing at (c) 300 °C and at (d) 500 °C for 1 h. (e–g) Co²⁺/(Co²⁺ + Co³⁺) ratio quantified for different probing depths in the LSC₁₁₃/LSC₂₁₄ trilayer film obtained by varying the detection angle, $f(\theta)$, at the photon energy of 3000 eV, and by varying the photon energy, $f(E_{\text{photon}})$, at the emission angle of 45°, shown for (e) the as-prepared state, and after annealing at (f) 300 °C and (g) 500 °C for 1 h. Co²⁺/(Co²⁺ + Co³⁺) qualitatively represents the relative presence of Co²⁺ in the films, which was calculated by fitting the satellite peaks as demonstrated in (a–d) for spectra collected at 15°. The probing depth is estimated as three times the inelastic mean free path of Co 2p_{3/2} photoelectrons (SI section S1). The colored rectangles mark the approximate position of the different layers, with blue for LSC₁₁₃, red for LSC₂₁₄, and gray for the STO substrate.

easily when they are adjacent to LSC₁₁₃ in the trilayers than their single phase counterparts. Our findings indicate that one can engineer the overall defect chemistry of a material by constructing superlattices with complementary defect behaviors, and thereby engineer the functionality.

2. METHODS

The LSC₁₁₃/LSC₂₁₄, LSC₁₁₃/LNO₂₁₄ trilayer and reference single phase films were grown by PLD using a KrF excimer laser with the wavelength 248 nm and a laser fluence of 1.9 J/cm². The number of pulses for the bottom LSC₁₁₃, LSC₂₁₄ or LNO₂₁₄, and top LSC₁₁₃ layers were 3450, 3000, and 3000, respectively. The deposition was carried out at 700 °C under 10 mTorr oxygen pressures. After the growth process, the films were cooled down to room temperature in 2 Torr oxygen pressure with a cooling rate of 5 °C/min.

The HAXPES experiment was carried out using the endstation located at the GALAXIES beamline of the SOLEIL synchrotron in

France. The photon energy covers the range 2.3 to 12 keV, and electrons with kinetic energies up to 12 keV can be analyzed.³⁷ The angle between the direction of the incident X-ray beam and the photoelectron detection is fixed to be 90°. The sample can be tilted to change the emission angle, as shown in Supporting Information (SI) Figure S1. Due to the large penetration depth of HAXPES, the C 1s peak is too weak to serve as the external peak calibration for spectra at small emission angles. Considering that the chemical environment of La is quite similar for all the layers and expected not to show any changes upon annealing, all the La 3d spectra in this work were aligned to be at 833.3 eV. The C 1s peak is at 284.8 eV when it is detectable for spectra with large emission angles (more surface sensitive). The HAXPES spectra were analyzed using the CasaXPS software. The (La + Sr)/Co ratios and Sr/La ratio were quantified based La 3d, Co 2p, and Sr 3d peaks. The Co valence states were identified from Co 2p peaks.

The lattice parameters of the trilayers and single phase films in their as-prepared condition and after annealing were measured by HRXRD

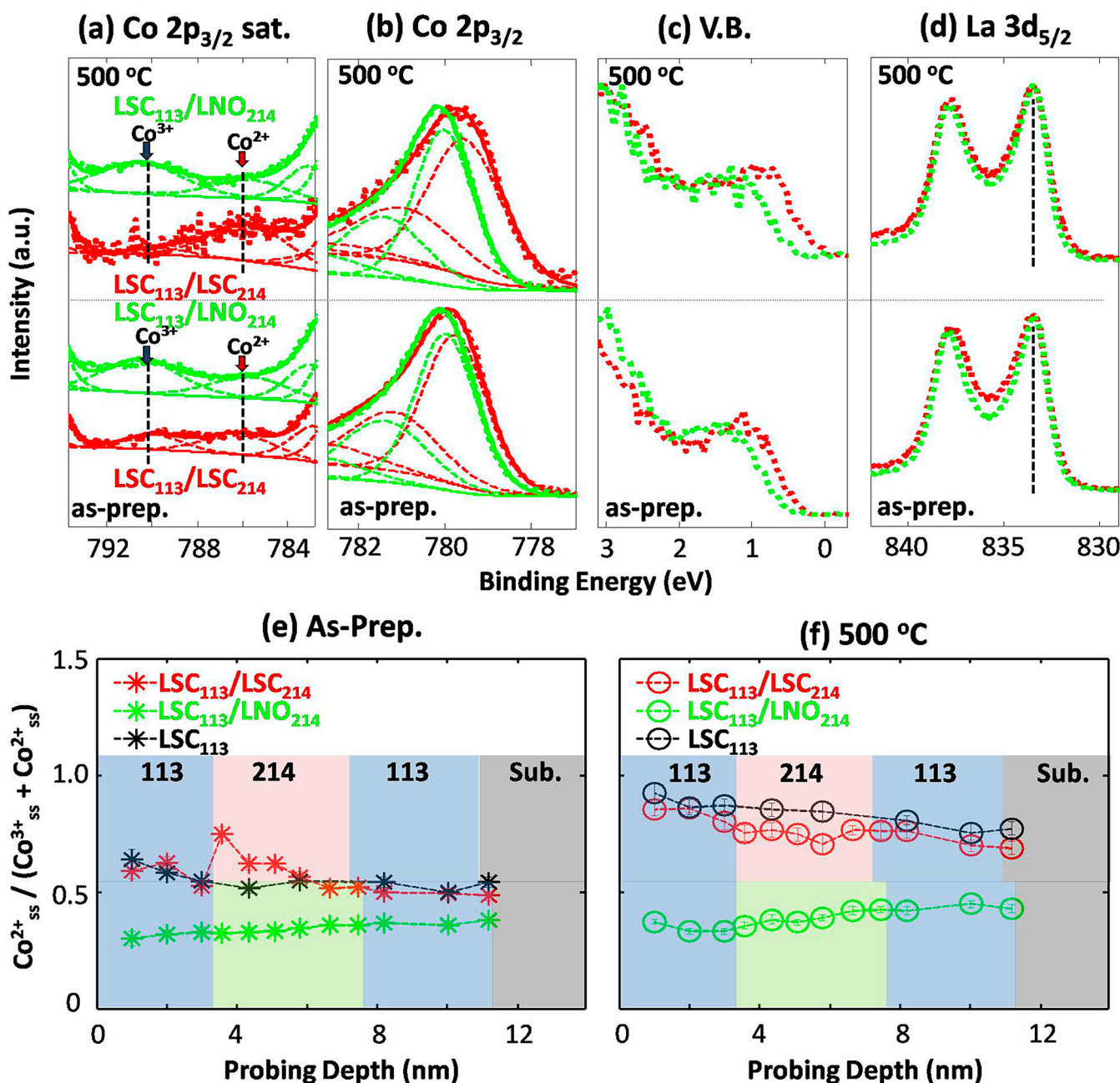


Figure 3. Comparison of the reduction of Co in LSC₁₁₃ in the LSC₁₁₃/LSC₂₁₄ and LSC₁₁₃/LNO₂₁₄ trilayers: (a–d): Co 2p_{3/2} satellite peak intensity (a), Co 2p_{3/2} main peak position (b), valence band (V.B.) spectra (c), and La 3d_{5/2} (d). The data shown in (a–d) were collected at 80° emission angle, corresponding to a probing depth within the top LSC₁₁₃ layer in the trilayers. The bottom two spectra in each panel are from the as-prepared samples, while the top spectra represent the state after annealing at 500 °C. (e–f) Comparison of Co²⁺/(Co²⁺ + Co³⁺) in the LSC₁₁₃ single phase reference film, and in the LSC₁₁₃/LSC₂₁₄ and LSC₁₁₃/LNO₂₁₄ trilayers, (e) in the as-prepared state and (f) after annealing at 500 °C. The probing depth is defined in the caption of Figure 2. The colored rectangles mark the approximate position of different layers, with blue for LSC₁₁₃, red for LSC₂₁₄, green for LNO₂₁₄, and gray for the STO substrate.

using a Rigaku Smartlab diffractometer equipped with a 2-bounce Ge (220) channel-cut monochromator and Cu Kα1 radiation.

Transmission electron microscopy (TEM) samples were fabricated in the Helios Nanolab 600 dual beam focused ion beam milling system. The Ga ion beam was operated at a voltage and current that was varied in a range of 30 keV–5 keV and 9.5 nA–28 pA, respectively. TEM measurements were performed using a JEOL 2010 FEG microscope. All the crystal structures in this manuscript are visualized using the Vesta software.³⁸

3. RESULTS AND DISCUSSION

3.1. LSC₁₁₃/LSC₂₁₄ and LSC₁₁₃/LNO₂₁₄ Trilayer Model Systems. LSC₁₁₃/LSC₂₁₄ and LSC₁₁₃/LNO₂₁₄ trilayer films grown by PLD were epitaxial with the substrate and had (001) out-of-plane orientation, as shown in the TEM images in Figure 1a. Based on the TEM images and X-ray reflectivity measurements, the thicknesses of each layer were 3–4 nm, with a total thickness of ~10 nm, as shown in Figure 1b. The samples were examined in their as-prepared state as well as after being reduced by annealing at 300 and 500 °C for 1 h at 10^{−10}

mbar in an ultrahigh vacuum chamber. A LSC_{113} film always served as the top layer in the trilayer structure to ensure that the oxygen surface exchange kinetics during the annealing for both types of trilayers were the same. The results were compared among these trilayers and single-phase ~ 10 nm-thick films of LSC_{113} , LSC_{214} , and LNO_{214} on STO (001) substrates, prepared under the same conditions.

3.2. Oxygen Defects across the Buried Interfaces Measured by HAXPES. We determined the transition metal valence states and cation composition by HAXPES in the thin film trilayers and across their interfaces. This information allowed us to compare the oxygen vacancy and oxygen interstitial content in the trilayer structures with respect to the single-phase thin film reference structures. Here, a decrease in the emission angle from 85° to 15° with respect to the surface normal implies an increase in probing depth. The probing depth at each emission angle and photon energy is defined as three times the inelastic mean free path, λ , of the photoelectron as described in SI section S1. The chemical information obtained by HAXPES at a given angle and photon energy is cumulative information from the top surface through different depths of the sample up to the maximum probing depth. For instance, the information obtained at 80° – 85° is mainly from the topmost LSC_{113} layers in the $\text{LSC}_{113}/\text{LSC}_{214}$ and in the $\text{LSC}_{113}/\text{LNO}_{214}$ trilayers; at an emission angle of 15° the spectra contain cumulative information extending from the surface into the STO substrate (Figure 2a).

First, we quantified the distribution of the Co valence state across the depth and buried interfaces of $\text{LSC}_{113}/\text{LSC}_{214}$ trilayer structures from the Co 2p photoelectron spectra measured as a function of photon energy and emission angle. The Co oxidation state is an important factor for determining the electronic and ionic conductivity of the LSC_{113} and LSC_{214} , as well as for the electron transfer process during oxygen reduction. Representative Co 2p spectra collected at different emission angles are shown in Figure 2a for the as-prepared $\text{LSC}_{113}/\text{LSC}_{214}$ trilayer. The Co 2p spectrum contains two main peaks, Co $2p_{1/2}$ and Co $2p_{3/2}$, corresponding to different spin–orbit couplings. For each main peak, there is also a satellite peak at higher binding energy because of the extra electrons transferred from the O 2p orbitals to the Co 3d orbital. These electrons screen the electric field of the holes in the Co 2p orbital created during the photoelectron emission process. The shape and position of the satellite peaks, particularly the Co $2p_{3/2}$ satellite peak, are widely used to identify the valence state of Co, as summarized in SI section S2. Under the preparation conditions during pulsed laser deposition of these films, the valence states of Co in LSC_{113} are predominantly $3+$ with a small amount of $4+$,^{39,40} while in LSC_{214} Co is mainly $3+$.⁴¹ After annealing in reducing conditions as described above, the $2+$ valence state of Co is expected to be part of the equilibrium in LSC_{113} ³⁹ and in LSC_{214} .⁴¹ The binding energies of the Co $2p_{3/2}$ satellite peak for Co^{2+} and for Co^{3+} are at ~ 786 eV^{42–46} and ~ 789 eV,^{42,47–49} respectively (Figure 2a, SI Table S1). To compare the Co valence state as a function of probing depth among different samples, we fitted the Co 2p spectra as shown in Figure 2. To qualitatively represent and compare the amount of Co^{2+} in the different films, we assessed the fractional presence of Co^{2+} , quantified as the ratio of the Co^{2+} $2p_{3/2}$ satellite peak area to the sum of the areas of the Co^{2+} and Co^{3+} $2p_{3/2}$ satellite peaks. This ratio is denoted as $\text{Co}_{\text{ss}}^{2+}/(\text{Co}_{\text{ss}}^{2+} + \text{Co}_{\text{ss}}^{3+})$. There is no evidence that the ratio of satellite peaks ($\text{Co}_{\text{ss}}^{2+}/\text{Co}_{\text{ss}}^{3+}$) increases linearly with the $\text{Co}^{2+}/\text{Co}^{3+}$ ratio.

However, it is known that higher peak intensity for the Co^{2+} satellite arises from a higher Co^{2+} content, and similarly for the Co^{3+} case (see references listed in SI Table S1), even if the ratio of satellite peak intensities does not have to be linear. Therefore, we did not make any conclusion about the absolute change of the $\text{Co}^{2+}/\text{Co}^{3+}$ ratio based on the satellite peak ratios in this manuscript. To reproduce the asymmetric shapes of the main peaks as accurately as possible and minimize their impact on the satellite peak quantification (Figure 2a), we fitted the Co $2p_{3/2}$ and Co $2p_{1/2}$ regions consistently with three peaks as performed in ref S0. It should be noted these three fitted peaks do not correspond to different valence states. More details on the fitting parameters can be found in SI section S3. The error bars in Figure 2 and in Figure 3 for $\text{Co}_{\text{ss}}^{2+}/(\text{Co}_{\text{ss}}^{2+} + \text{Co}_{\text{ss}}^{3+})$ represent the uncertainty introduced by the fitting procedure. The impact of different fitting parameters, including fitting range, peak shape, and position, on the final result were evaluated, and the standard deviation of the fitting results was used to show the uncertainty introduced by the fitting procedure. Considering the fact that we did all the measurements during the same beam time at the same end-station at SOLEIL synchrotron, we believe that the uncertainty arising from measurement conditions, such as the fluctuation of beam intensity or the measurement geometry, is negligible in comparing the samples to each other.

The $\text{Co}_{\text{ss}}^{2+}/(\text{Co}_{\text{ss}}^{2+} + \text{Co}_{\text{ss}}^{3+})$ ratio quantified either as a function of emission angle, $f(\theta)$, or as a function of photon energy, $f(E_{\text{photon}})$, is plotted versus probing depth in Figure 2e–g. As shown in SI section S1, the probing depth is estimated as three times the inelastic mean free path of Co 2p $3/2$ photoelectrons. Each point contains cumulative information from the top surface to the probing depth. A general increase in the Co^{2+} content at each depth can be seen after annealing the specimen at 300 and 500 $^\circ\text{C}$ at a low oxygen pressure. This is consistent with the annealing induced reduction and creation of oxygen vacancies in the LSC_{113} and LSC_{214} layers. Concurrent with the increased intensity of the Co^{2+} $2p_{3/2}$ satellite peak, the Co main peak position also shifted to lower binding energies (SI Figure S4b). The increase of the $\text{Co}_{\text{ss}}^{2+}/(\text{Co}_{\text{ss}}^{2+} + \text{Co}_{\text{ss}}^{3+})$ ratio is more evident in the LSC_{113} layers after annealing at 500 $^\circ\text{C}$; here $\text{Co}_{\text{ss}}^{2+}/(\text{Co}_{\text{ss}}^{2+} + \text{Co}_{\text{ss}}^{3+})$ decreases slightly when the main sampling region enters into the LSC_{214} layer and increases again when entering the bottom LSC_{113} layer (Figure 2g). This effect is observed because LSC_{214} is more difficult to reduce by forming oxygen vacancies (i.e., it has a higher oxygen vacancy formation energy) than LSC_{113} .^{27,36} Finally, it is worth reminding that, while the plots in Figure 2e–g show a spatially varying profile, the HAXPES intrinsically measures accumulated data from the surface into varying depths in the samples, and so the final nonzero values for $\text{Co}_{\text{ss}}^{2+}/(\text{Co}_{\text{ss}}^{2+} + \text{Co}_{\text{ss}}^{3+})$ should not be interpreted as the presence of Co^{2+} in the STO substrate.

Having demonstrated that HAXPES enables profiling of the Co valence state across the buried heterointerfaces of the $\text{LSC}_{113}/\text{LSC}_{214}$ trilayer, we now examine the valence state of Co in LSC_{113} when it is adjacent to two different oxides, i.e. either LSC_{214} or LNO_{214} within the two trilayer structures. A direct examination of all the Co $2p_{3/2}$ peaks and the valence band edge (in Figure 3a, b, c) reveals the dependence of the Co valence state in LSC_{113} on the neighboring layer. First, the Co^{2+} $2p_{3/2}$ satellite peak intensity is higher for LSC_{113} with LSC_{214} as the neighboring oxide than the one with LNO_{214} , both at the as-prepared state and after annealing at 500 $^\circ\text{C}$ (Figure 3a). Second, the main Co $2p_{3/2}$ peak of LSC_{113} neighboring with

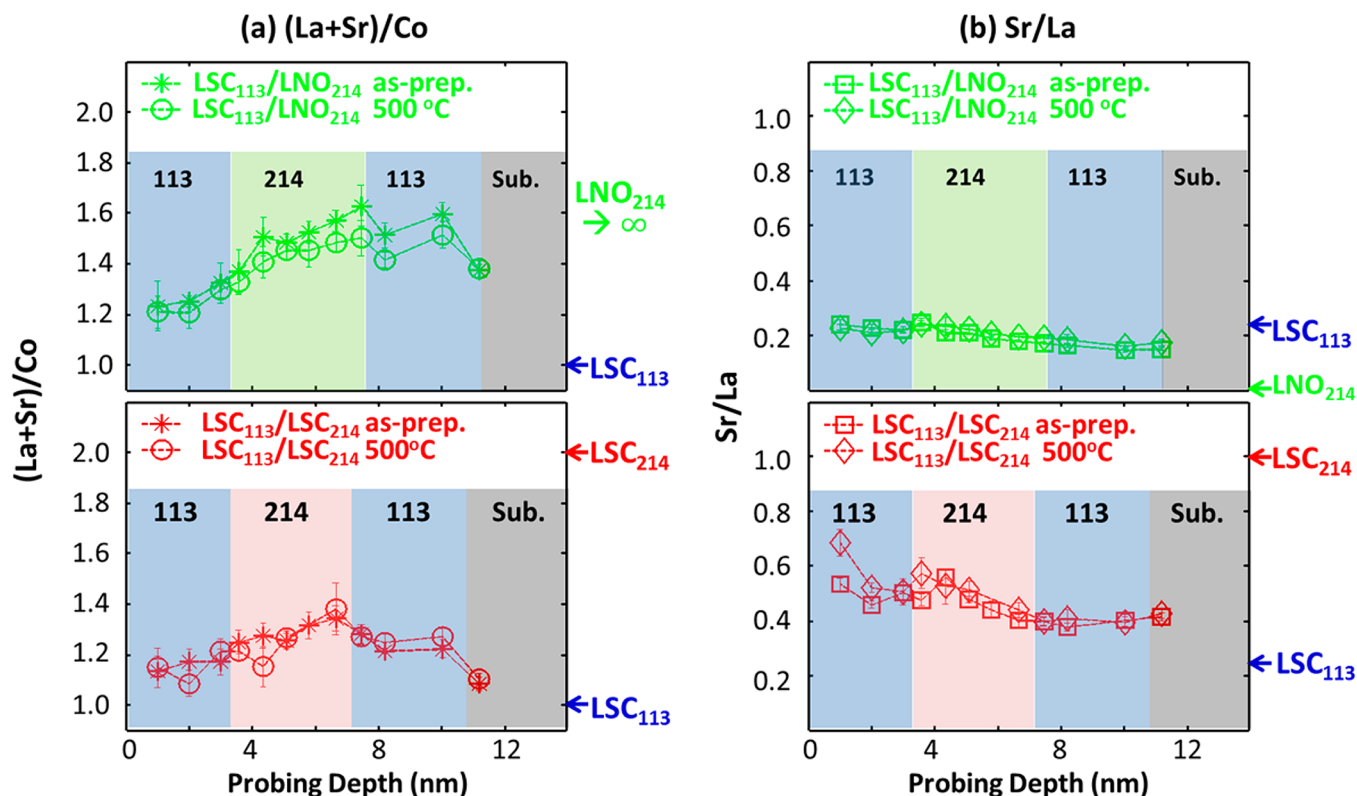


Figure 4. Comparison of cation compositions in the $\text{LSC}_{113}/\text{LSC}_{214}$ and $\text{LSC}_{113}/\text{LNO}_{214}$ trilayers. Depth profiles of (a) $(\text{La} + \text{Sr})/\text{Co}$ and (b) Sr/La in the as-prepared state and after annealing at 500°C . The composition quantification were based on the $\text{Sr } 3d$, $\text{La } 3d$, $\text{Co } 2p$ photoelectron spectra collected at emission angles from 15° to 85° using 3000 eV photons. The cation compositions are plotted as a function of probing depth which was defined in the caption of Figure 2. The $(\text{La} + \text{Sr})/\text{Co}$ and Sr/La represent cumulative data from the surface into the depth of the samples until the probing depth.

LSC_{214} is located at a lower binding energy than that of LSC_{113} neighboring with LNO_{214} (Figure 3b). Third, the valence band edge in LSC_{113} was also impacted by the neighboring oxide layer. When the LSC_{113} film is reduced at elevated temperatures and low oxygen pressures, formation of oxygen vacancies induce defect states and shift the valence band edge up.^{36,51–53} The valence band edge of LSC_{113} with LSC_{214} and of LSC_{113} with LNO_{214} both up-shifted (i.e., to lower binding energy) after annealing at 500°C (Figure 3c). This upshift is larger for LSC_{113} with LSC_{214} , indicating a more significant reduction of Co in the LSC_{113} layer when it neighbors LSC_{214} . All three of these results are consistent among each other and indicate a more reduced Co in LSC_{113} when adjacent to LSC_{214} than when it is adjacent to LNO_{214} . It is worth also noting that the $\text{La } 3d$ core level emission from LSC_{113} does not depend on the composition of the neighboring oxide (Figure 3d).

More quantitatively, the $\text{Co}_{\text{ss}}^{2+}/(\text{Co}_{\text{ss}}^{2+} + \text{Co}_{\text{ss}}^{3+})$ ratio in LSC_{113} neighboring with LSC_{214} is higher than that in LSC_{113} neighboring with LNO_{214} for both the as-prepared state and after annealing at 500°C (Figure 3e, f). The amounts of Co^{2+} in both the top and the bottom LSC_{113} layers in the $\text{LSC}_{113}/\text{LSC}_{214}$ trilayer significantly increase after annealing at 500°C (Figure 3e, f). However, the amount of Co^{2+} in the $\text{LSC}_{113}/\text{LNO}_{214}$ trilayer only slightly increases after annealing at 500°C (Figure 3f). The $\text{Co}_{\text{ss}}^{2+}/(\text{Co}_{\text{ss}}^{2+} + \text{Co}_{\text{ss}}^{3+})$ ratios in the LSC_{113} single phase reference film and in the LSC_{113} layer of the $\text{LSC}_{113}/\text{LSC}_{214}$ trilayer are very similar to each other. Any difference in the reduced states of these two specimens was not possible to resolve by HAXPES, but was more clearly resolved by the HRXRD measurements that are presented later.

Due to the strong overlap between the $\text{Ni } 2p$ and $\text{La } 3d$ peaks, and between the $\text{Ni } 3p$ and $\text{Co } 3p$ peaks (SI Figure S8), the Ni valence state in the LNO_{214} layers could not be determined from HAXPES. However, the results obtained from HRXRD measurements (discussed later in the paper) can be used to examine the relative reducibility of Ni in the reference LNO_{214} film and in the $\text{LSC}_{113}/\text{LNO}_{214}$ trilayer structure.

It is interesting that the $\text{Co}_{\text{ss}}^{2+}/(\text{Co}_{\text{ss}}^{2+} + \text{Co}_{\text{ss}}^{3+})$ ratio was high near the first interface (Figure 2e), indicating possibly a quite high Co^{2+} concentration in that region in the as-prepared state. This situation may arise because of Sr enrichment near the $\text{LSC}_{113}/\text{LSC}_{214}$ interface after high temperature synthesis, as previously reported by another group.³⁴ However, it is only one data point that showed very high Co^{2+} content for the as-prepared state, and we will show in the later section we ruled out the possibility of Sr migration as the possible mechanism of different defect chemistry in the trilayer structure.

Having shown that the Co valence state in LSC_{113} depends significantly on the neighboring oxide (LSC_{214} versus LNO_{214}), we must address whether such a difference arises from changes in the local oxygen nonstoichiometry or in the local cation chemistry. The $(\text{La} + \text{Sr})/\text{Co}$ ratios in the $\text{LSC}_{113}/\text{LSC}_{214}$ and $\text{LSC}_{113}/\text{LNO}_{214}$ trilayers are similar before and after annealing at 500°C (Figure 4a), indicating no structural changes should be expected after annealing. (The relative sensitivity factors for La , Sr and Co were obtained by measuring the composition of 80 nm thick LSC_{113} films grown at the same conditions (SI section S1).) More important for the Co valence state is the Sr/La ratio because a change in the Sr doping level could be charge-compensated by a change in the Co valence state and in

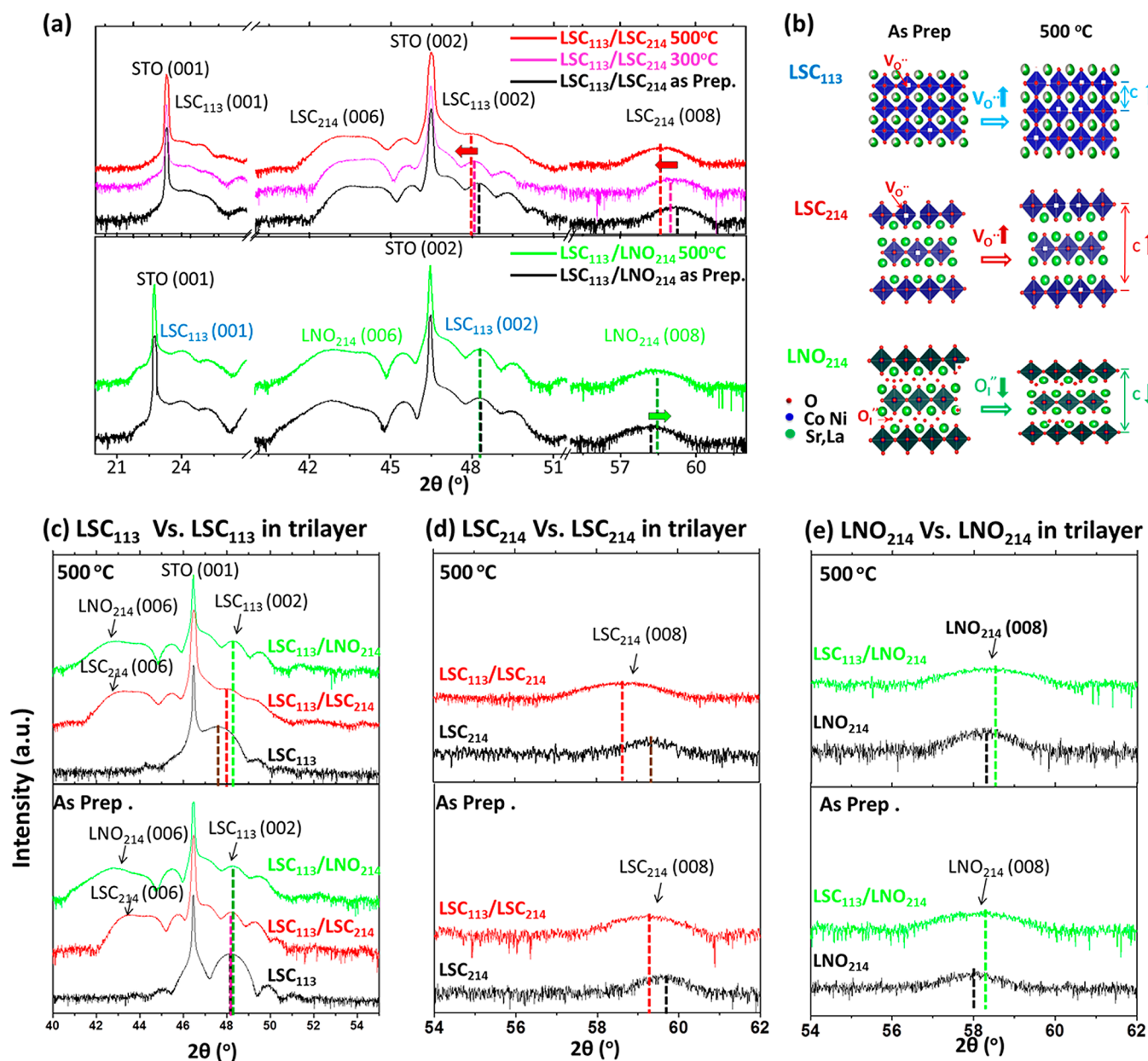


Figure 5. Lattice expansion and contraction due to oxygen nonstoichiometry change, quantified by HRXRD in LSC₁₁₃/LSC₂₁₄, LSC₁₁₃/LNO₂₁₄ trilayer structures and their single phase counterparts. (a) 2θ - ω scans of LSC₁₁₃/LSC₂₁₄ (top) and LSC₁₁₃/LNO₂₁₄ (bottom), as-prepared and after annealing at 300 and 500 °C for 1 h. (b) The schematics show the expansion of the c lattice parameter in LSC₁₁₃ and LSC₂₁₄ films due to the increase of oxygen vacancies, and the contraction of c in LNO₂₁₄ due to the loss of oxygen interstitials after annealing. (c–e) Comparison of the HRXRD patterns to show the relative changes in the out-of-plane lattice parameter, c , in LSC₁₁₃, LSC₂₁₄, and LNO₂₁₄: (c) LSC₁₁₃ (002) peak in 2θ - ω scans for LSC₁₁₃, LSC₁₁₃/LSC₂₁₄, and LSC₁₁₃/LNO₂₁₄, as-prepared and after annealing at 500 °C. (d) LSC₂₁₄ (008) and (e) LNO₂₁₄ (008) peaks in 2θ - ω scans for the single phase and trilayer structures in the as-prepared state and after annealing at 500 °C. The dashed lines mark the position of the LSC₁₁₃ (002) peak, LSC₂₁₄ (008) peak, and LNO₂₁₄ (008) peak.

the oxygen vacancy concentration.^{40,54} As shown in Figure 4b, the Sr/La ratio in the as-prepared LSC₁₁₃/LSC₂₁₄ film decreases as the probing depth goes from the top surface into the bulk. This is due to the Sr enrichment at/near the surface, a phenomenon that is generally observed for doped perovskite oxides.^{51,55–57} After 500 °C, the Sr/La distribution remains unchanged for the LSC₁₁₃/LNO₂₁₄ trilayer, and it increases mainly at the very top surface of the LSC₁₁₃/LSC₂₁₄ trilayer. On the other hand, the Co²⁺ fraction clearly increased within the LSC₁₁₃/LSC₂₁₄ trilayer after annealing at 500 °C (Figure 3e, f). If the enrichment of Sr²⁺ on the La-site were the only change in chemistry at 500 °C, then we should have found a more

oxidized Co in LSC₁₁₃, but we found a more reduced Co. Therefore, the more reduced Co is consistent with an overall increase of oxygen vacancy concentration within the LSC₁₁₃/LSC₂₁₄ trilayers to an extent significantly greater than that in the LSC₁₁₃/LNO₂₁₄ trilayer (Figure 3e, f). Lastly, we note that one reason why the (La + Sr)/Co ratio in LSC₁₁₃/LNO₂₁₄ and LSC₁₁₃/LSC₂₁₄ are larger than 1 is that the chemical information obtained by HAXPES is a cumulative information across different depths of the sample. Even when the probing depth, here referring to three times the inelastic mean free path λ , is mainly within the top LSC₁₁₃ layer, the data carry also some information from the underlying LSC₂₁₄ or LNO₂₁₄. This

Table 1. Comparison of the c Lattice Parameter, the Change in the c Lattice Parameter (Δc), in the Out-of-Plane Strain State, ϵ ($\Delta c/c$), and in the Oxygen Nonstoichiometry ($\Delta\delta$) in $\text{La}_{0.8}\text{Sr}_{0.2}\text{CoO}_{3-\delta}$ (LSC₁₁₃), $(\text{La}_{0.5}\text{Sr}_{0.5})_2\text{CoO}_{4-\delta}$ (LSC₂₁₄), and $\text{La}_2\text{NiO}_{4+\delta}$ (LNO₂₁₄) in Trilayer Structures and in Single Phase Films after Annealing at 500 °C

Sample	Condition	c (Å)	Δc (Å)	ϵ	$\Delta\delta$	$\Delta\delta_{\text{trilayer}} - \Delta\delta_{\text{single phase}}$
LSC ₁₁₃ single phase	As Prep	3.770				
	500 °C	3.810	0.040	0.011	0.188	
LSC ₁₁₃ in LSC ₁₁₃ /LSC ₂₁₄	As Prep.	3.768				
	500 °C	3.789	0.021	0.006	0.120	−0.068
LSC ₁₁₃ in LSC ₁₁₃ /LNO ₂₁₄	As Prep.	3.764				
	500 °C	3.764	0.000	0.000	0.000	−0.188
LSC ₂₁₄ single phase	As Prep.	12.40				
	500 °C	12.44	0.037	0.003	0.074	
LSC ₂₁₄ in LSC ₁₁₃ /LSC ₂₁₄	As Prep.	12.46				
	500 °C	12.57	0.117	0.009	0.173	0.099
LNO ₂₁₄ single phase	As Prep	12.71				
	500 °C	12.67	−0.040	−0.003	−0.038	
LNO ₂₁₄ in LSC ₁₁₃ /LNO ₂₁₄	As Prep.	12.66				
	500 °C	12.58	−0.082	−0.006	−0.079	−0.041

can also explain the seemingly larger (La + Sr)/Co ratio (and smaller Sr/La ratio) in LSC₁₁₃/LNO₂₁₄ compared to that in LSC₁₁₃/LSC₂₁₄. Considering that HAXPES is always more sensitive to the surface, Sr enrichment on the surface of LSC₁₁₃ mentioned above can also lead to an A to B ratio larger than 1 for both LSC₁₁₃/LSC₂₁₄ and LSC₁₁₃/LNO₂₁₄.

In summary, combining the information on the Co valence state (Figures 2 and 3) and the cation composition (Figure 4) deduced from HAXPES, we found that the Co in LSC₁₁₃ neighboring LSC₂₁₄ (in LSC₁₁₃/LSC₂₁₄) is more reducible than the Co in LSC₁₁₃ neighboring LNO₂₁₄ (in LSC₁₁₃/LNO₂₁₄). This is because of a larger concentration of oxygen vacancies that form in LSC₁₁₃ of the LSC₁₁₃/LSC₂₁₄ than in LSC₁₁₃ of the LSC₁₁₃/LNO₂₁₄, after annealing at elevated temperatures in a reducing atmosphere. From this finding, we can conclude that the oxygen nonstoichiometry in thin LSC₁₁₃ layers can be significantly influenced by the nature of the adjacent oxide.

3.3. Oxygen Defect States Probed by HRXRD. The oxygen nonstoichiometry in transition metal oxides impacts the lattice parameter, commonly referred to as chemical strain.^{58,59} In this section, we present results from HRXRD analysis. We quantify the relative changes in the lattice parameters in LSC₁₁₃/LSC₂₁₄ and LSC₁₁₃/LNO₂₁₄ trilayers and relate the lattice expansion or contraction to the relative changes in the oxygen nonstoichiometry. This approach for observing the oxygen defect chemistry in thin films and buried layers is complementary to the HAXPES analysis presented in the previous section.

The LSC₁₁₃, LSC₂₁₄, LNO₂₁₄ layers within the LSC₁₁₃/LSC₂₁₄ and LSC₁₁₃/LNO₂₁₄ trilayers remained epitaxial with the STO (001) substrate before and after annealing (Figure 5a). After annealing at 500 °C for 1 h, the out-of-plane lattice parameter, c , of LSC₁₁₃ in LSC₁₁₃/LSC₂₁₄ expanded by 0.6% (Figure 5a, Table 1), while that of LSC₁₁₃ in LSC₁₁₃/LNO₂₁₄ did not show any detectable change. The c for LSC₁₁₃ in the single phase film is larger than that for either of the trilayer structures, both in the as-prepared state and after 500 °C annealing (Figure 5c). The lattice parameter of LSC₁₁₃ is known^{60,61} to increase with oxygen nonstoichiometry (δ), i.e., with the oxygen vacancy concentration, as depicted schematically in Figure 5b. The lattice parameter and oxygen nonstoichiometry of the as-prepared samples and after heating at temperature T were defined to be $c_{\text{as-prep}}$, $\delta_{\text{as-prep}}$, c_T , and δ_T .

To relate the change in the lattice parameter ($\Delta c = c_T - c_{\text{as-prep}}$) to the relative changes in the oxygen nonstoichiometry ($\Delta\delta = \delta_T - \delta_{\text{as-prep}}$), we used the chemical expansion coefficient, $\frac{\partial \epsilon}{\partial \delta} = 0.053$ and $\frac{\partial^2 \epsilon}{\partial \delta^2} = 1.543$, where $\epsilon = \frac{\Delta c}{c}$ and $\chi_v = \frac{\delta}{3}$, quantified by Chen et al.⁶⁰ for $\text{La}_{0.8}\text{Sr}_{0.2}\text{CoO}_{3-\delta}$ (SI section S3). The c lattice parameter and the annealing-induced changes in the c (Δc) and in the oxygen nonstoichiometric ($\Delta\delta$) for LSC₁₁₃ single phase, LSC₁₁₃ in LSC₁₁₃/LSC₂₁₄, and LSC₁₁₃ in LSC₁₁₃/LNO₂₁₄ are shown in Table 1. We note that, in relating the Δc to $\Delta\delta$ above, the chemical expansion coefficient deduced for bulk powder specimens was used.⁶⁰ Furthermore, we also included the impact of the in-plane clamping by the substrate, by calculating how the chemical expansion should propagate into changes in c for clamped films, using an approximate Young's modulus and Poisson ratios as shown in SI section S3. For the LSC₁₁₃ in LSC₁₁₃/LNO₂₁₄, the $\Delta\delta$ after 500 °C was too small to be detected by our HRXRD measurement. The $\Delta\delta$ for single phase LSC₁₁₃ after 500 °C is estimated to be 0.188, which is larger than that of LSC₁₁₃ in the LSC₁₁₃/LSC₂₁₄ and the LSC₁₁₃/LNO₂₁₄ trilayers.

For RP phases, it is known that the c lattice parameter decreases when the oxide loses oxygen interstitials, but it increases when the oxide loses lattice oxygen and forms oxygen vacancies^{62–65} (SI Figure S10). We found that the c parameter of LSC₂₁₄ increased after annealing in reducing conditions, while the c parameter of LNO₂₁₄ decreased (Figure 5a, b, Table 1). For LSC₂₁₄ with 50% Sr used in this study, the oxygen vacancy is the dominant defect for the conditions involved in the preparation and annealing of these films.⁴¹ The dominant oxygen defect in LNO₂₁₄, however, is oxygen interstitials, even at temperatures as high as 900 °C and under reducing conditions of 10^{-11} bar oxygen partial pressure.⁶³ Therefore, we can conclude that, in this work after annealing at 500 °C, the LSC₂₁₄ has a higher concentration of oxygen vacancies, while the LNO₂₁₄ has a lower concentration of oxygen interstitials. Compared with the one in the LSC₁₁₃/LSC₂₁₄ trilayer structure, single phase LSC₂₁₄ has a smaller c lattice parameter (Figure 5d, Table 1). On the other hand, the LNO₂₁₄ single phase shows a larger c than that in the LSC₁₁₃/LNO₂₁₄ trilayer (Figure 5e). These results indicate more oxygen vacancies are present in the LSC₂₁₄ and less oxygen interstitials are present in LNO₂₁₄ films when they are in contact with LSC₁₁₃ in the trilayers. To relate

the lattice parameter changes to relative changes in the oxygen nonstoichiometry ($\Delta\delta$), we used the chemical expansion coefficient $\left(\frac{\partial c}{\partial \delta}\right)_T = 0.62 \text{ \AA}$, quantified for bulk LNO_{214} .⁶³

The $\Delta\delta$ in LNO_{214} from the as-prepared state to the 500 °C annealed state is estimated to be about -0.079 for LNO_{214} in the trilayer and about -0.038 for single phase LNO_{214} (Table 1). For LSC_{214} , there has been no quantitative study of its chemical expansion behavior. Under our experimental (deposition and annealing) conditions, the dominant oxygen defects are oxygen vacancies and the reducible cation is Co in both LSC_{113} and LSC_{214} . Therefore, it is reasonable to assume the same chemical expansion coefficient for the conversion of the change in the lattice parameter to the change in the oxygen nonstoichiometry in the LSC_{113} and LSC_{214} films. With this assumption, the LSC_{214} in the trilayer structure has $\Delta\delta = 0.173$ after annealing 500 °C, while the LSC_{214} single phase layer has $\Delta\delta = 0.074$. It is possible that these phases actually have different chemical expansion coefficients, so the $\Delta\delta$ estimated for LSC_{214} above may have some uncertainty. Nevertheless, the overall conclusion that the LSC_{214} in trilayers have more oxygen vacancies than the LSC_{214} single phase layer remains valid. The comparison of $\Delta\delta$ values shows that both the LSC_{214} and the LNO_{214} lose more oxygen when they are in contact with LSC_{113} in the trilayers than their single phase counterparts.

In summary, measurements of the c lattice parameters in the trilayers and single phase films showed that a different level of oxygen substoichiometry can be equilibrated in LSC_{113} depending on the nature of the neighboring oxide. The c lattice parameter of LSC_{113} in $\text{LSC}_{113}/\text{LSC}_{214}$ increased after annealing at elevated temperatures, correlating to a clear increase in oxygen vacancy concentration. On the other hand, the c lattice parameter in LSC_{113} in $\text{LSC}_{113}/\text{LNO}_{214}$ did not show any detectable change after annealing, indicating that the oxygen vacancy concentration change in LSC_{113} is smaller than the detection limit by these HRXRD measurements. This result is consistent with the HAXPES results, which showed an easier reducibility of LSC_{113} with LSC_{214} than of LSC_{113} with LNO_{214} as the neighboring oxide.

3.4. Possible Mechanism for Interface-Dependent Defect Chemistry. The reason for the different oxygen nonstoichiometry levels in the LSC_{113} single phase versus when it is in the two trilayers is likely the different electrostatic potentials built near the heterointerfaces of the trilayers. After annealing under low oxygen pressure, oxide films tend to lose oxygen to the environment and show a reduction in electronegativity, the energy difference between the Fermi level and the vacuum energy.^{52,53,66} Our previous work showed that the defect state formed at elevated temperatures within the energy band of LSC_{113} led to an increase of Fermi energy and a metallic-like band structure.^{27,36} Under the same conditions, LSC_{214} phase alone had much less changes in electronic structure and oxygen vacancy content.³⁶ The difference in electronic structure of LSC_{113} and LSC_{214} leads to a band level as illustrated in Figure 6a for LSC_{113} and LSC_{214} individually, if the two phases were not in contact. Bringing these two phases into contact at their interface can build up a negative and a positive electrostatic potential in LSC_{214} and LSC_{113} , respectively, and drive the Fermi levels of LSC_{214} and LSC_{113} to align across the interface, as sketched in Figure 6b). Such an upshift of the LSC_{214} Fermi level by contacting with LSC_{113} was observed in our previous experimental work.²⁷ Similar

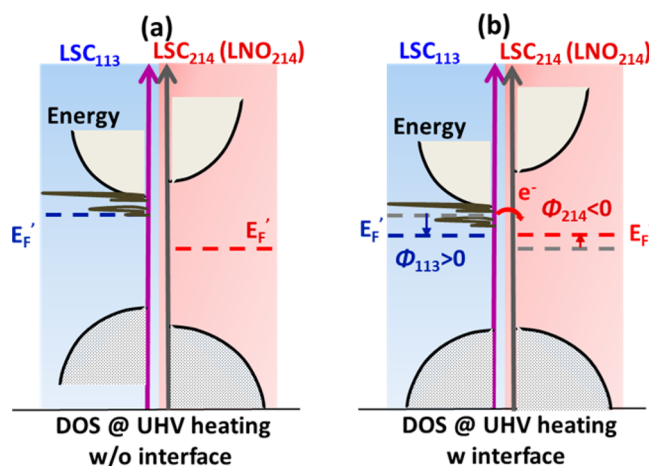


Figure 6. Illustration of how the presence of $\text{LSC}_{113}/\text{LSC}_{214}$ and $\text{LSC}_{113}/\text{LNO}_{214}$ interfaces leads to the creation of a local electric field, which can impact the local oxygen defect equilibria. (a) The misalignment of the Fermi level in LSC_{113} and LSC_{214} (LNO_{214}) single phases after losing oxygen by annealing at high temperature, if each phase were considered separately. (b) The alignment of the Fermi level in LSC_{113} and LSC_{214} (LNO_{214}) annealing by the creation of local electric field, ϕ , upon annealing. The black lines below the conduction band in b and c refer to the defect states created upon formation of oxygen vacancies at high temperature.

arguments can be applied to the LSC_{113} and LNO_{214} heterostructure.

The formation energies of oxygen vacancies, $V_{\text{O}}(E_{\text{F}})$, and of oxygen interstitials, $O_{\text{i}}(E_{\text{F}})$, are described by the following equations:^{2,67–69}

$$E_{\text{F}} = E_{\text{def}} + \mu - E_{\text{perf}} + qE_{\text{F}} + q\phi \quad q = 2e \quad (1)$$

$$E_{\text{F}} = E_{\text{def}} - \mu - E_{\text{perf}} + qE_{\text{F}} + q\phi \quad q = -2e \quad (2)$$

where E_{def} and E_{perf} are the energies of the system with and without oxygen defects, respectively; μ is the chemical potential of oxygen in the materials; q is the charge for oxygen defect; E_{F} is the Fermi energy; and ϕ is the electrostatic potential. A positive ϕ in LSC_{113} leads to an increase of oxygen vacancy formation energy and less oxygen vacancies near the heterointerface with LSC_{214} or LNO_{214} . A negative ϕ equilibrates in LSC_{214} and in LNO_{214} and decreases the oxygen vacancy formation energy while increasing the oxygen interstitial formation energy. This leads to more oxygen vacancies in LSC_{214} and less oxygen interstitials in LNO_{214} near their interface with LSC_{113} . The magnitude of such an electrostatic potential at the interface does not have to be large to introduce significant changes in the oxygen nonstoichiometry (δ).^{4,61} As shown quantitatively in SI section 4, less than a 0.1 eV electrostatic potential near the interface can introduce the observed change in the oxygen nonstoichiometry in LSC_{113} between the trilayer structure and the single phase (i.e., $\Delta\delta$ of 0.188 in Table 1). A way to detect the presence of such an electrostatic potential is to measure the shifts in the binding energy of the core level peaks in XPS. However, the shift in peak positions in the photoelectron spectra introduced by such small electrostatic potentials (<0.1 eV) is beyond the resolution limits of the measurements in this work, in part due to the strong overlap between the La, Co, and Ni peaks. Further investigation on other multilayer systems that consist of elements whose core level spectra do not overlap is currently

ongoing to confirm the existence of an electrostatic potential near the perovskite-related heterointerfaces. If the model above is correct, one should expect the LSC_{113} in $\text{LSC}_{113}/\text{LSC}_{214}$ and $\text{LSC}_{113}/\text{LNO}_{214}$ trilayers to lose less oxygen than the single phase LSC_{113} , and the LSC_{214} and LNO_{214} in trilayers to lose more oxygen than the single-phase films. This is what is observed in Figure 5c–e. All of these results support the explanation we proposed above, that the existence of an electrostatic potential near the heterointerfaces can change the defect chemistry in the thin layers of LSC_{113} , LSC_{214} , and LNO_{214} . In the model we proposed above, the driving force for charged defect distribution affects not only electron transfer from LSC_{113} across the interface to LSC_{214} or LNO_{214} but also exchange and re-equilibration of charged oxygen defects. Consistent with the electron transfer direction, the interstitial oxygens (-2 formal charge) within LNO_{214} can transfer to LSC_{113} , leading to less oxygen vacancies ($+2$ formal charge) in LSC_{113} .

It is also worth noting that the Sr/La ratio increased slightly at the very top surface of the $\text{LSC}_{113}/\text{LSC}_{214}$ trilayer after 500 °C annealing. Furthermore, the increase of Sr at the A-site of LSC_{113} is known to increase the oxygen vacancy concentration in LSC_{113} .³⁹ The possible diffusion of Sr from LSC_{214} into LSC_{113} might also explain the higher oxygen vacancies for LSC_{113} in $\text{LSC}_{113}/\text{LSC}_{214}$ than $\text{LSC}_{113}/\text{LNO}_{214}$. However, it cannot explain why LSC_{113} in the $\text{LSC}_{113}/\text{LSC}_{214}$ has less oxygen vacancies than the LSC_{113} single phase. Therefore, we believe the electrostatic potential near the interface as described above is more likely to be behind the change in oxygen defect chemistry instead of Sr interdiffusion.

In the description of the oxygen defect formation energy above, we assumed that $E_{\text{def}} - E_{\text{perf}}$ in eqs 1 and 2 is the same for the single phase and near the heterointerface. This quantity can in fact also be affected by the symmetry breaking and alteration of coordination and bond energies near the interface.⁷⁰ While we do not rule out this interface chemistry related effect, calculating the difference in $E_{\text{def}} - E_{\text{perf}}$ for single phase versus heterointerface is beyond the scope of this work. Furthermore, in this paper we did not consider the effect of strain which is known to impact the oxygen defect chemistry.⁵¹ This is because all our films are very thin (~ 10 nm in total). As a result, the in-plane lattice parameter of all the films are determined by the substrate, leading to very similar in-plane lattice parameters for both the single phase films and the trilayer films. Lastly, it is worth noting that besides oxygen defects, the defect chemistry for other ions can also be strongly influenced by the presence of the interface, as shown by Xu et al. for the intercalation energy of Li in the $\text{Li}_x\text{FePO}_4/\text{Li}_x\text{MPO}_4$ heterostructure.²³

3.5. Perspectives and Implications of the Phenomenon. The fabrication and operation of many oxide devices involve elevated temperatures, reactive gas environments, and the presence of an external bias. Such external drivers can change the oxygen nonstoichiometry in oxides, leading to different electronic structures, conductivities, and magnetic properties. The ability to change the response of oxygen defects to the environment presents a new way of tailoring the functionality of transition metal oxides. For example, tensile strain is now known to be one way to lower the oxygen vacancy or interstitial formation energy, leading to the ability to accommodate more oxygen vacancies or interstitials, and eventually faster oxygen exchange kinetics at elevated temperatures.^{51,71–73}

To tune the oxygen defects and functionality of oxide heterostructures, we proposed to couple the defect chemistry and electronic structure of two oxides through their interface. Depending on the neighboring oxide, one can either suppress or enhance the oxygen defect formation under an electrostatic driving force arising internally from the interface. In this work, we showed that by placing LSC_{113} next to LNO_{214} , oxygen vacancy formation in LSC_{113} was strongly suppressed. One key parameter is the relative Fermi level positions of the two phases upon the change of their oxygen nonstoichiometry due to the external driving force (here the annealing temperature), finally forming an internal driving force (here the interface electrostatic potential). Based on the rigid band theory of Lankhorst et al.,⁶⁶ the Fermi level of LSC_{113} corresponds to the gradual filling up of states in a broad electron band with electrons introduced by oxygen vacancy formation. One needs similar models that correlate oxygen nonstoichiometry to the Fermi level in different materials so that the neighboring oxides could be chosen for controlling the oxygen defects. Our results point out “band engineering” as a potential way of tailoring defect chemistry and generating different functionalities in oxide superlattices. We are currently working on other heterostructures that consist of different RP phase materials to further confirm the impact of band engineering through heterointerfaces on the defect chemistry of those materials.

In this work, we used a combination of HAXPES and HRXRD to probe the relative oxygen nonstoichiometry levels in $\text{LSC}_{113}/\text{LSC}_{214}$ and $\text{LSC}_{113}/\text{LNO}_{214}$ trilayer structures. This approach is nondestructive and does not require a complicated sample preparation, and it can therefore be used for materials that are sensitive to electron beam damage. Several recent studies have shown the significant impact of heterointerfaces on local electronic structure and transport properties. Chen et al.⁷⁴ and Huijben et al.⁷⁵ reported enhanced electronic mobility by inserting a single-unit cell of $\text{La}_{1-x}\text{Sr}_x\text{MnO}_3$ ($x = 0, 1/8$, and $1/3$)⁷⁴ and SrCuO_3 between LaAlO_3 and SrTiO_3 . The resulting enhanced mobility was tied to potential changes in oxygen defect chemistry induced by the inserted layer. Yajima et al.⁷⁶ succeeded in tuning the band alignment in perovskite metal–semiconductor heterojunctions over a broad range of 1.7 eV by inserting a few unit cells of either LaTiO_3 or SrAlO_x between the SrRuO_3 and Nb:SrTiO_3 . However, the impact of the interface on the oxygen defects accompanied by such a large change in electrostatic field was not discussed. The methods used in the work can be easily adapted to other systems, including those mentioned above, to clarify the role of local oxygen defects in determining the novel properties that arise near oxide heterointerfaces, such as magneto-electric coupling,¹⁰ interfacial superconductivity,^{11,12} high electronic and ionic conductivity,^{13,14,74–76} and catalytic activity.^{15–23} Furthermore, this approach can be extended to *in situ* studies at elevated temperatures, in reactive gas environments, and under electrochemical potentials to probe more quantitatively how the local defects evolve when the chemical potential of the gas phase is changed. This can be particularly useful for the applications to high temperature electrochemical energy conversion or to redox-reaction based resistive memories.

4. CONCLUSION

Interfaces of perovskite and Ruddlesden–Popper type oxides present an interesting case for affecting the defect chemistry of each phase through their interfaces. We used a novel combination of HAXPES and HRXRD to probe the local

oxygen defect distribution across the buried interfaces of $\text{LSC}_{113}/\text{LSC}_{214}$ and $\text{LSC}_{113}/\text{LNO}_{214}$ trilayer model systems. From HAXPES measurements, we found that the Co in the LSC_{113} adjacent to LSC_{214} is more reducible than the Co in the LSC_{113} adjacent to LNO_{214} . This is because of a larger concentration of oxygen vacancies that form in LSC_{113} of the $\text{LSC}_{113}/\text{LSC}_{214}$ than that in LSC_{113} of the $\text{LSC}_{113}/\text{LNO}_{214}$ after annealing in a reducing atmosphere. The HRXRD results indicated consistent behavior as found from HAXPES. Reduction-induced chemical expansion of the LSC_{113} single phase was larger than that of LSC_{113} adjacent to LSC_{214} or to LNO_{214} . The comparison of lattice parameters upon reduction indicated that the $\Delta\delta$ in LSC_{113} adjacent to LNO_{214} was less than that in LSC_{113} adjacent to LSC_{214} and in the LSC_{113} single phase. On the other hand, LSC_{214} and LNO_{214} were found to lose more oxygen when in contact with the LSC_{113} layer compared to their single phase counterparts. Our results demonstrated that the oxygen defect chemistry of these transition metal oxides was strongly impacted by the presence of interfaces and the properties of the adjacent phases. We attributed this behavior to the electrostatic potentials built near the heterointerfaces. In this work, combining HAXPES with HRXRD, we provide a nondestructive way to qualitatively probe the local oxygen defect states in transition metal oxide heterostructures. Our results also point out interface engineering as a potential way to control the local defect chemistry, electronic structure, and functionality for oxide superlattices.

■ ASSOCIATED CONTENT

Supporting Information

The Supporting Information is available free of charge on the ACS Publications website at DOI: [10.1021/acs.chemmater.8b00808](https://doi.org/10.1021/acs.chemmater.8b00808).

S1 Probing depth of hard X-ray photoelectron spectroscopy (HAXPES); S2 Identifying Co valence state using photoelectron spectroscopy (PES); S3 Quantifying oxygen nonstoichiometry change in $\text{LSC}_{113}/\text{LSC}_{214}$ and $\text{LSC}_{113}/\text{LNO}_{213}$ trilayers based on chemical expansion; S4 Estimating oxygen nonstoichiometry change introduced by the interface electrostatic potential (PDF)

■ AUTHOR INFORMATION

Corresponding Author

*E-mail: byildiz@mit.edu.

ORCID

Yan Chen: 0000-0001-6193-7508

Present Address

[§]Guangzhou Key Laboratory for Surface Chemistry of Energy Materials, New Energy Institute, School of Environment and Energy, South China University of Technology, 382 East Road, University City, Guangzhou 510006, P. R. China.

Notes

The authors declare no competing financial interest.

■ ACKNOWLEDGMENTS

Authors acknowledge the US-DOE - Basic Energy Sciences, Grant No. DE-SC0002633 for financial support. Y.C. acknowledges additional support from the Schlumberger Foundation Faculty for the Future fellowship. D.D.F. was supported by the U.S. Department of Energy (DOE), Office of Science, Office of Basic Energy Sciences (BES), Division of Materials Science and

Engineering. The authors acknowledge useful discussions with Dr. Christian Lenser and Dr. Mostafa Youssef. This work made use of the MRSEC Shared Experimental Facilities at MIT, supported by the National Science Foundation under Award Number DMR - 1419807.

■ REFERENCES

- (1) Ganduglia-Pirovano, M. V.; Hofmann, A.; Sauer, J. Oxygen vacancies in transition metal and rare earth oxides: Current state of understanding and remaining challenges. *Surf. Sci. Rep.* **2007**, *62*, 219–270.
- (2) Tuller, H. L.; Bishop, S. R. Tailoring Material Properties through Defect Engineering. *Chem. Lett.* **2010**, *39*, 1226–1231.
- (3) Freysoldt, C.; Grabowski, B.; Hickel, T.; Neugebauer, J.; Kresse, G.; Janotti, A.; Van de Walle, C. G. First-principles calculations for point defects in solids. *Rev. Mod. Phys.* **2014**, *86*, 253–305.
- (4) Chen, D.; Tuller, H. L. Voltage-Controlled Nonstoichiometry in Oxide Thin Films: $\text{Pr}_{0.1}\text{Ce}_{0.9}\text{O}_{2-\delta}$ Case Study. *Adv. Funct. Mater.* **2014**, *24*, 7638–7644.
- (5) Kalinin, S. V.; Spaldin, N. A. Functional Ion Defects in Transition Metal Oxides. *Science* **2013**, *341*, 858–859.
- (6) Kalinin, S. V.; Borisevich, A.; Fong, D. Beyond Condensed Matter Physics on the Nanoscale: The Role of Ionic and Electrochemical Phenomena in the Physical Functionalities of Oxide Materials. *ACS Nano* **2012**, *6*, 10423–10437.
- (7) Kosacki, I.; Suzuki, T.; Anderson, H. U.; Colomban, P. Raman scattering and lattice defects in nanocrystalline CeO_2 thin films. *Solid State Ionics* **2002**, *149*, 99–105.
- (8) Rupp, J. L. M.; Fabbri, E.; Marrocchelli, D.; Han, J. W.; Chen, D.; Traversa, E.; Tuller, H. L.; Yildiz, B. Scalable Oxygen-Ion Transport Kinetics in Metal-Oxide Films: Impact of Thermally Induced Lattice Compaction in Acceptor Doped Ceria Films. *Adv. Funct. Mater.* **2014**, *24*, 1562–1574.
- (9) Schweiger, S.; Kubicek, M.; Messerschmitt, F.; Murer, C.; Rupp, J. L. M. A Microdot Multilayer Oxide Device: Let Us Tune the Strain-Ionic Transport Interaction. *ACS Nano* **2014**, *8*, 5032–5048.
- (10) Bauer, U.; Emori, S.; Beach, G. S. D. Voltage-controlled domain wall traps in ferromagnetic nanowires. *Nat. Nanotechnol.* **2013**, *8*, 411–416.
- (11) Ohtomo, A.; Muller, D. A.; Grazul, J. L.; Hwang, H. Y. Artificial charge-modulation in atomic-scale perovskite titanate superlattices. *Nature* **2002**, *419*, 378–380.
- (12) Hwang, H. Y.; Iwasa, Y.; Kawasaki, M.; Keimer, B.; Nagaosa, N.; Tokura, Y. Emergent phenomena at oxide interfaces. *Nat. Mater.* **2012**, *11*, 103–113.
- (13) Maier, J. Nanoionics: ionic charge carriers in small systems. *Phys. Chem. Chem. Phys.* **2009**, *11*, 3011–22.
- (14) Fabbri, E.; Pergolesi, D.; Traversa, E. Ionic conductivity in oxide heterostructures: the role of interfaces. *Sci. Technol. Adv. Mater.* **2010**, *11*, 054503.
- (15) Li, G. H.; Gray, K. A. The solid-solid interface: Explaining the high and unique photocatalytic reactivity of TiO_2 -based nanocomposite materials. *Chem. Phys.* **2007**, *339*, 173–187.
- (16) Sase, M.; Hermes, F.; Yashiro, K.; Sato, K.; Mizusaki, J.; Kawada, T.; Sakai, N.; Yokokawa, H. Enhancement of oxygen surface exchange at the hetero-interface of $(\text{La,Sr})\text{CoO}_3/(\text{La,Sr})_2\text{CoO}_4$ with PLD-Layered films. *J. Electrochem. Soc.* **2008**, *155*, B793–B797.
- (17) Sase, M.; Yashiro, K.; Sato, K.; Mizusaki, J.; Kawada, T.; Sakai, N.; Yamaji, K.; Horita, T.; Yokokawa, H. Enhancement of oxygen exchange at the hetero interface of $(\text{La,Sr})\text{CoO}_3/(\text{La,Sr})_2\text{CoO}_4$ in composite ceramics. *Solid State Ionics* **2008**, *178*, 1843–1852.
- (18) Hayd, J.; Yokokawa, H.; Ivers-Tiffée, E. Hetero-Interfaces at Nanoscaled $(\text{La,Sr})\text{CoO}_{3-\delta}$ Thin-Film Cathodes Enhancing Oxygen Surface-Exchange Properties. *J. Electrochem. Soc.* **2013**, *160*, F351–F359.
- (19) Yashiro, K.; Nakamura, T.; Sase, M.; Hermes, F.; Sato, K.; Kawada, T.; Mizusaki, J. Composite Cathode of Perovskite-Related

Oxides, $(\text{La,Sr})\text{CoO}_{3-\delta}/(\text{La,Sr})_2\text{CoO}_{4+\delta}$ for Solid Oxide Fuel Cells. *Electrochem. Solid-State Lett.* **2009**, *12*, B135–B137.

(20) Crumlin, E. J.; Mutoro, E.; Ahn, S. J.; la O, G. J.; Leonard, D. N.; Borisevich, A.; Biegalski, M. D.; Christen, H. M.; Shao-Horn, Y. Oxygen Reduction Kinetics Enhancement on a Heterostructured Oxide Surface for Solid Oxide Fuel Cells. *J. Phys. Chem. Lett.* **2010**, *1*, 3149–3155.

(21) Ivanov, D. V.; Pinaeva, L. G.; Isupova, L. A.; Sadovskaya, E. M.; Prosvirin, I. P.; Gerasimov, E. Y.; Yakovleva, I. S. Effect of surface decoration with LaSrFeO_4 on oxygen mobility and catalytic activity of $\text{La}_{0.4}\text{Sr}_{0.6}\text{FeO}_{3-\delta}$ in high-temperature N_2O decomposition, methane combustion and ammonia oxidation. *Appl. Catal., A* **2013**, *457*, 42–51.

(22) Stacchiola, D. J.; Senanayake, S. D.; Liu, P.; Rodriguez, J. A. Fundamental Studies of Well-Defined Surfaces of Mixed-Metal Oxides: Special Properties of $\text{MO}_x/\text{TiO}_2(110)$ $\{M = \text{V}, \text{Ru}, \text{Ce}, \text{or W}\}$. *Chem. Rev.* **2013**, *113*, 4373–4390.

(23) Xu, S.; Jacobs, R.; Wolverton, C.; Kuech, T.; Morgan, D. Nanoscale Voltage Enhancement at Cathode Interfaces in Li-Ion Batteries. *Chem. Mater.* **2017**, *29*, 1218–1229.

(24) Herpers, A.; Lenser, C.; Park, C.; Offi, F.; Borgatti, F.; Panaccione, G.; Menzel, S.; Waser, R.; Dittmann, R. Spectroscopic Proof of the Correlation between Redox-State and Charge-Carrier Transport at the Interface of Resistively Switching Ti/PCMO Devices. *Adv. Mater.* **2014**, *26*, 2730–2735.

(25) Kim, Y. M.; He, J.; Biegalski, M. D.; Ambaye, H.; Lauter, V.; Christen, H. M.; Pantelides, S. T.; Pennycook, S. J.; Kalinin, S. V.; Borisevich, A. Y. Probing oxygen vacancy concentration and homogeneity in solid-oxide fuel-cell cathode materials on the subunit-cell level. *Nat. Mater.* **2012**, *11*, 888–894.

(26) Kim, Y. M.; Morozovska, A.; Eliseev, E.; Oxley, M. P.; Mishra, R.; Selbach, S. M.; Grande, T.; Pantelides, S. T.; Kalinin, S. V.; Borisevich, A. Y. Direct observation of ferroelectric field effect and vacancy-controlled screening at the $\text{BiFeO}_3/\text{La}_x\text{Sr}_{1-x}\text{MnO}_3$ interface. *Nat. Mater.* **2014**, *13*, 1019–1025.

(27) Tsvetkov, N.; Chen, Y.; Yildiz, B. Reducibility of Co at the $\text{La}_{0.8}\text{Sr}_{0.2}\text{CoO}_3/(\text{La}_{0.5}\text{Sr}_{0.5})_2\text{CoO}_4$ hetero-interface at elevated temperatures. *J. Mater. Chem. A* **2014**, *2*, 14690–14695.

(28) Chambers, S. A., Probing Perovskite Interfaces and Superlattices with X-ray Photoemission Spectroscopy. In *Hard X-ray Photoelectron Spectroscopy (HAXPES)*; Woicik, C. J., Ed.; Springer International Publishing: Cham, 2016; pp 341–380.

(29) Slooten, E.; Zhong, Z.; Molegraaf, H. J. A.; Eerkes, P. D.; de Jong, S.; Masee, F.; van Heumen, E.; Kruize, M. K.; Wenderich, S.; Kleibeuker, J. E.; Gorgoi, M.; Hilgenkamp, H.; Brinkman, A.; Huijben, M.; Rijnders, G.; Blank, D. H. A.; Koster, G.; Kelly, P. J.; Golden, M. S. Hard x-ray photoemission and density functional theory study of the internal electric field in $\text{SrTiO}_3/\text{LaAlO}_3$ oxide heterostructures. *Phys. Rev. B: Condens. Matter Mater. Phys.* **2013**, *87*, 085128.

(30) Chen, Y. Z.; Bovet, N.; Trier, F.; Christensen, D. V.; Qu, F. M.; Andersen, N. H.; Kasama, T.; Zhang, W.; Giraud, R.; Dufouleur, J.; Jespersen, T. S.; Sun, J. R.; Smith, A.; Nygård, J.; Lu, L.; Büchner, B.; Shen, B. G.; Linderth, S.; Pryds, N. A high-mobility two-dimensional electron gas at the spinel/perovskite interface of $\gamma\text{-Al}_2\text{O}_3/\text{SrTiO}_3$. *Nat. Commun.* **2013**, *4*, 1371.

(31) Chronos, A.; Yildiz, B.; Tarancon, A.; Parfitt, D.; Kilner, J. A. Oxygen diffusion in solid oxide fuel cell cathode and electrolyte materials: mechanistic insights from atomistic simulations. *Energy Environ. Sci.* **2011**, *4*, 2774–2789.

(32) Tarancon, A.; Burriel, M.; Santiso, J.; Skinner, S. J.; Kilner, J. A. Advances in layered oxide cathodes for intermediate temperature solid oxide fuel cells. *J. Mater. Chem.* **2010**, *20*, 3799–3813.

(33) Han, J. W.; Yildiz, B. Mechanism for enhanced oxygen reduction kinetics at the $(\text{La,Sr})\text{CoO}_{3-\delta}/(\text{La,Sr})_2\text{CoO}_{4+\delta}$ hetero-interface. *Energy Environ. Sci.* **2012**, *5*, 8598–8607.

(34) Feng, Z.; Yacoby, Y.; Gadre, M. J.; Lee, Y.-L.; Hong, W. T.; Zhou, H.; Biegalski, M. D.; Christen, H. M.; Adler, S. B.; Morgan, D.; Shao-Horn, Y. Anomalous Interface and Surface Strontium Segregation in $(\text{La}_{1-y}\text{Sr}_y)_2\text{CoO}_{4+\delta}/\text{La}_{1-x}\text{Sr}_x\text{CoO}_{3-\delta}$ Heterostructured Thin Films. *J. Phys. Chem. Lett.* **2014**, *5*, 1027–1034.

(35) Gadre, M. J.; Lee, Y. L.; Morgan, D. Cation interdiffusion model for enhanced oxygen kinetics at oxide heterostructure interfaces. *Phys. Chem. Chem. Phys.* **2012**, *14*, 2606–2616.

(36) Chen, Y.; Cai, Z. H.; Kuru, Y.; Ma, W.; Tuller, H. L.; Yildiz, B. Electronic Activation of Cathode Superlattices at Elevated Temperatures - Source of Markedly Accelerated Oxygen Reduction Kinetics. *Adv. Energy Mater.* **2013**, *3*, 1221–1229.

(37) Rueff, J. P.; Ablett, J. M.; Ceolin, D.; Prieur, D.; Moreno, T.; Baledent, V.; Lassalle-Kaiser, B.; Rault, J. E.; Simon, M.; Shukla, A. The GALAXIES beamline at the SOLEIL synchrotron: inelastic X-ray scattering and photoelectron spectroscopy in the hard X-ray range. *J. Synchrotron Radiat.* **2015**, *22*, 175–179.

(38) Momma, K.; Izumi, F. VESTA 3 for three-dimensional visualization of crystal, volumetric and morphology data. *J. Appl. Crystallogr.* **2011**, *44*, 1272–1276.

(39) Mizusaki, J.; Mima, Y.; Yamauchi, S.; Fueki, K.; Tagawa, H. Nonstoichiometry of the perovskite-type oxides $\text{La}_{1-x}\text{Sr}_x\text{CoO}_{3-\delta}$. *J. Solid State Chem.* **1989**, *80*, 102–111.

(40) Madhukar, S.; Aggarwal, S.; Dhote, A. M.; Ramesh, R.; Krishnan, A.; Keeble, D.; Poindexter, E. Effect of oxygen stoichiometry on the electrical properties of $\text{La}_{0.5}\text{Sr}_{0.5}\text{CoO}_3$ electrodes. *J. Appl. Phys.* **1997**, *81*, 3543–3547.

(41) Vashook, V. V.; Ullmann, H.; Olshevskaya, O. P.; Kulik, V. P.; Lukashevich, V. E.; Kokhanovskij, L. V. Composition and electrical conductivity of some cobaltates of the type $\text{La}_{2-x}\text{Sr}_x\text{CoO}_{4.5-x/2\pm\delta}$. *Solid State Ionics* **2000**, *138*, 99–104.

(42) Galakhov, V. R.; Karelina, V. V.; Kellerman, D. G.; Gorshkov, V. S.; Ovechkin, N. A.; Neumann, M. Electronic structure, X-ray spectra, and magnetic properties of the LiCoO_2 -delta and NaCoO_2 nonstoichiometric oxides. *Phys. Solid State* **2002**, *44*, 266–273.

(43) Chuang, T. J.; Brundle, C. R.; Rice, D. W. Interpretation of the x-ray photoemission spectra of cobalt oxides and cobalt oxide surfaces. *Surf. Sci.* **1976**, *59*, 413–429.

(44) Petitto, S. C.; Marsh, E. M.; Carson, G. A.; Langell, M. A. Cobalt oxide surface chemistry: The interaction of $\text{CoO}(100)$, $\text{Co}_3\text{O}_4(110)$ and $\text{Co}_3\text{O}_4(111)$ with oxygen and water. *J. Mol. Catal. A: Chem.* **2008**, *281*, 49–58.

(45) Gu, Z. J.; Xiang, X.; Fan, G. L.; Li, F. Facile Synthesis and Characterization of Cobalt Ferrite Nanocrystals via a Simple Reduction-Oxidation Route. *J. Phys. Chem. C* **2008**, *112*, 18459–18466.

(46) Brabers, V. A. M.; van Setten, F. X-ray photoelectron spectroscopy study of the ionic configuration of the spinel CuMnCoO_4 . *J. Phys. D: Appl. Phys.* **1983**, *16*, L169–L172.

(47) Oku, M. X-ray photoelectron spectrum of low-spin Co(III) in LiCoO_2 . *J. Solid State Chem.* **1978**, *23*, 177–185.

(48) Moses, A. W.; Flores, H. G. G.; Kim, J. G.; Langell, M. A. Surface properties of LiCoO_2 , LiNiO_2 and $\text{LiNi}_{1-x}\text{Co}_x\text{O}_2$. *Appl. Surf. Sci.* **2007**, *253*, 4782–4791.

(49) Galenda, A.; Natile, M. M.; Krishnan, V.; Bertagnolli, H.; Glisenti, A. LaSrCoFeO and $\text{Fe}_2\text{O}_3/\text{LaSrCoFeO}$ powders: Synthesis and characterization. *Chem. Mater.* **2007**, *19*, 2796–2808.

(50) Biesinger, M. C.; Payne, B. P.; Grosvenor, A. P.; Lau, L. W. M.; Gerson, A. R.; Smart, R. S. Resolving surface chemical states in XPS analysis of first row transition metals, oxides and hydroxides: Cr, Mn, Fe, Co and Ni. *Appl. Surf. Sci.* **2011**, *257*, 2717–2730.

(51) Cai, Z. H.; Kuru, Y.; Han, J. W.; Chen, Y.; Yildiz, B. Surface Electronic Structure Transitions at High Temperature on Perovskite Oxides: The Case of Strained $\text{La}_{0.8}\text{Sr}_{0.2}\text{CoO}_3$ Thin Films. *J. Am. Chem. Soc.* **2011**, *133*, 17696–17704.

(52) Deskins, N. A.; Rousseau, R.; Dupuis, M. Defining the Role of Excess Electrons in the Surface Chemistry of TiO_2 . *J. Phys. Chem. C* **2010**, *114*, 5891–5897.

(53) Greiner, M. T.; Helander, M. G.; Tang, W. M.; Wang, Z. B.; Qiu, J.; Lu, Z. H. Universal energy-level alignment of molecules on metal oxides. *Nat. Mater.* **2012**, *11*, 76–81.

(54) Mizusaki, J.; Tabuchi, J.; Matsuura, T.; Yamauchi, S.; Fueki, K. Electrical Conductivity and Seebeck Coefficient of Nonstoichiometric $\text{La}_{1-x}\text{Sr}_x\text{CoO}_{3-\delta}$. *J. Electrochem. Soc.* **1989**, *136*, 2082–2088.

- (55) Lee, W.; Han, J. W.; Chen, Y.; Cai, Z.; Yildiz, B. Cation Size Mismatch and Charge Interactions Drive Dopant Segregation at the Surfaces of Manganite Perovskites. *J. Am. Chem. Soc.* **2013**, *135*, 7909–7925.
- (56) Dulli, H.; Dowben, P. A.; Liou, S. H.; Plummer, E. W. Surface segregation and restructuring of colossal-magnetoresistant manganese perovskites $\text{La}_{0.65}\text{Sr}_{0.35}\text{MnO}_3$. *Phys. Rev. B: Condens. Matter Mater. Phys.* **2000**, *62*, R14629–R14632.
- (57) Chen, Y.; Téllez, H.; Burriel, M.; Yang, F.; Tsvetkov, N.; Cai, Z.; McComb, D. W.; Kilner, J. A.; Yildiz, B. Segregated Chemistry and Structure on (001) and (100) Surfaces of $(\text{La}_{1-x}\text{Sr}_x)_2\text{CoO}_4$ Override the Crystal Anisotropy in Oxygen Exchange Kinetics. *Chem. Mater.* **2015**, *27*, S436–S450.
- (58) Swallow, J. G.; Woodford, W. H.; Chen, Y.; Lu, Q.; Kim, J. J.; Chen, D.; Chiang, Y. M.; Carter, W. C.; Yildiz, B.; Tuller, H. L.; Van Vliet, K. J. Chemomechanics of ionically conductive ceramics for electrical energy conversion and storage. *J. Electroceram.* **2014**, *32*, 3–27.
- (59) Marrocchelli, D.; Bishop, S. R.; Tuller, H. L.; Watson, G. W.; Yildiz, B. Charge localization increases chemical expansion in cerium-based oxides. *Phys. Chem. Chem. Phys.* **2012**, *14*, 12070–12074.
- (60) Chen, X. Y.; Yu, J. S.; Adler, S. B. Thermal and chemical expansion of Sr-doped lanthanum cobalt oxide $(\text{La}_{1-x}\text{Sr}_x\text{CoO}_{3-\delta})$. *Chem. Mater.* **2005**, *17*, 4537–4546.
- (61) Biegalski, M. D.; Crumlin, E.; Belianinov, A.; Mutoro, E.; Shao-Horn, Y.; Kalinin, S. V. In situ examination of oxygen non-stoichiometry in $\text{La}_{0.80}\text{Sr}_{0.20}\text{CoO}_{3-\delta}$ thin films at intermediate and low temperatures by x-ray diffraction. *Appl. Phys. Lett.* **2014**, *104*, 161910.
- (62) Nakamura, T.; Yashiro, K.; Sato, K.; Mizusaki, J. Defect chemical and statistical thermodynamic studies on oxygen nonstoichiometric $\text{Nd}_{2-x}\text{Sr}_x\text{NiO}_{4+\delta}$. *Solid State Ionics* **2009**, *180*, 1406–1413.
- (63) Nakamura, T.; Yashiro, K.; Sato, K.; Mizusaki, J. Structural analysis of $\text{La}_{2-x}\text{Sr}_x\text{NiO}_{4+\delta}$ by high temperature X-ray diffraction. *Solid State Ionics* **2010**, *181*, 292–299.
- (64) Kharton, V. V.; Kovalevsky, A. V.; Avdeev, M.; Tsepis, E. V.; Patrakeev, M. V.; Yaremchenko, A. A.; Naumovich, E. N.; Frade, J. R. Chemically induced expansion of $\text{La}_2\text{NiO}_{4+\delta}$ -based materials. *Chem. Mater.* **2007**, *19*, 2027–2033.
- (65) Moggi, L. V.; Prado, F. D.; Cuello, G. J.; Caneiro, A. Study of the Crystal Chemistry of the $n = 2$ Ruddlesden-Popper Phases $\text{Sr}_3\text{FeMO}_{6+\delta}$ ($M = \text{Fe}, \text{Co}, \text{and Ni}$) Using in Situ High Temperature Neutron Powder Diffraction. *Chem. Mater.* **2009**, *21*, 2614–2623.
- (66) Lankhorst, M. H. R.; Bouwmeester, H. J. M.; Verweij, H. Use of the rigid band formalism to interpret the relationship between O chemical potential and electron concentration in $\text{La}_{1-x}\text{Sr}_x\text{CoO}_{3-\delta}$. *Phys. Rev. Lett.* **1996**, *77*, 2989–2992.
- (67) Bristowe, N. C.; Littlewood, P. B.; Artacho, E. Surface defects and conduction in polar oxide heterostructures. *Phys. Rev. B: Condens. Matter Mater. Phys.* **2011**, *83*, 205405.
- (68) Ingram, B. J.; Eastman, J. A.; Chang, K. C.; Kim, S. K.; Fister, T. T.; Perret, E.; You, H.; Baldo, P. M.; Fuoss, P. H. In situ x-ray studies of oxygen surface exchange behavior in thin film $\text{La}_{0.6}\text{Sr}_{0.4}\text{Co}_{0.2}\text{Fe}_{0.8}\text{O}_{3-\delta}$. *Appl. Phys. Lett.* **2012**, *101*, 051603.
- (69) Yu, L. P.; Zunger, A. A polarity-induced defect mechanism for conductivity and magnetism at polar-nonpolar oxide interfaces. *Nat. Commun.* **2014**, *5*, 5118.
- (70) Yang, J.; Youssef, M.; Yildiz, B. Predicting point defect equilibria across oxide hetero-interfaces: model system of $\text{ZrO}_2/\text{Cr}_2\text{O}_3$. *Phys. Chem. Chem. Phys.* **2017**, *19*, 3869–3883.
- (71) Kubicek, M.; Cai, Z. H.; Ma, W.; Yildiz, B.; Hutter, H.; Fleig, J. Tensile Lattice Strain Accelerates Oxygen Surface Exchange and Diffusion in $\text{La}_{1-x}\text{Sr}_x\text{CoO}_{3-\delta}$ Thin Films. *ACS Nano* **2013**, *7*, 3276–3286.
- (72) Tsvetkov, N.; Lu, Q. Y.; Chen, Y.; Yildiz, B. Accelerated Oxygen Exchange Kinetics on $\text{Nd}_2\text{NiO}_{4+\delta}$ Thin Films with Tensile Strain along c-Axis. *ACS Nano* **2015**, *9*, 1613–1621.
- (73) Kushima, A.; Yip, S.; Yildiz, B. Competing strain effects in reactivity of LaCoO_3 with oxygen. *Phys. Rev. B: Condens. Matter Mater. Phys.* **2010**, *82*, 115435.
- (74) Chen, Y. Z.; Trier, F.; Wijnands, T.; Green, R. J.; Gauquelin, N.; Egoavil, R.; Christensen, D. V.; Koster, G.; Huijben, M.; Bovet, N.; Macke, S.; He, F.; Sutarto, R.; Andersen, N. H.; Sulpizio, J. A.; Honig, M.; Prawiroatmodjo, G.; Jespersen, T. S.; Linderroth, S.; Ilani, S.; Verbeeck, J.; Van Tendeloo, G.; Rijnders, G.; Sawatzky, G. A.; Pryds, N. Extreme mobility enhancement of two-dimensional electron gases at oxide interfaces by charge-transfer-induced modulation doping. *Nat. Mater.* **2015**, *14*, 801–806.
- (75) Huijben, M.; Koster, G.; Kruize, M. K.; Wenderich, S.; Verbeeck, J.; Bals, S.; Slooten, E.; Shi, B.; Molegraaf, H. J. A.; Kleibeuker, J. E.; van Aert, S.; Goedkoop, J. B.; Brinkman, A.; Blank, D. H. A.; Golden, M. S.; van Tendeloo, G.; Hilgkamp, H.; Rijnders, G. Defect Engineering in Oxide Heterostructures by Enhanced Oxygen Surface Exchange. *Adv. Funct. Mater.* **2013**, *23*, 5240–5248.
- (76) Yajima, T.; Hikita, Y.; Minohara, M.; Bell, C.; Mundy, J. A.; Kourkoutis, L. F.; Muller, D. A.; Kumigashira, H.; Oshima, M.; Hwang, H. Y. Controlling band alignments by artificial interface dipoles at perovskite heterointerfaces. *Nat. Commun.* **2015**, *6*, 6759.